EUROPEAN SYNCHROTRON RADIATION FACILITY

INSTALLATION EUROPEENNE DE RAYONNEMENT SYNCHROTRON

Experiment Report Form

The double page inside this form is to be filled in by all users or groups of users who have had access to beam time for measurements at the ESRF.

Once completed, the report should be submitted electronically to the User Office via the User Portal:
https://wwws.esrf.fr/misapps/SMISWebClient/protected/welcome.do

Deadlines for submission of Experimental Reports

Experimental reports must be submitted within the period of 3 months after the end of the experiment.

Experiment Report supporting a new proposal ("relevant report")

If you are submitting a proposal for a new project, or to continue a project for which you have previously been allocated beam time, you must submit a report on each of your previous measurement(s):

- even on those carried out close to the proposal submission deadline (it can be a *"preliminary report"),*
- even for experiments whose scientific area is different form the scientific area of the new proposal,
- carried out on CRG beamlines.

You must then register the report(s) as "relevant report(s)" in the new application form for beam time.

Deadlines for submitting a report supporting a new proposal

- 1st March Proposal Round - **5th March**
- 10th September Proposal Round - **13th September**

The Review Committees reserve the right to reject new proposals from groups who have not reported on the use of beam time allocated previously.

Reports on experiments relating to long term projects

Proposers awarded beam time for a long term project are required to submit an interim report at the end of each year, irrespective of the number of shifts of beam time they have used.

Published papers

All users must give proper credit to ESRF staff members and proper mention to ESRF facilities which were essential for the results described in any ensuing publication. Further, they are obliged to send to the Joint ESRF/ ILL library the complete reference and the abstract of all papers appearing in print, and resulting from the use of the ESRF.

Should you wish to make more general comments on the experiment, please note them on the User Evaluation Form, and send both the Report and the Evaluation Form to the User Office.

Instructions for preparing your Report

- fill in a separate form for each project or series of measurements.
- type your report in English.
- include the experiment number to which the report refers.
- make sure that the text, tables and figures fit into the space available.
- if your work is published or is in press, you may prefer to paste in the abstract, and add full reference details. If the abstract is in a language other than English, please include an English translation.

ESRF	**Experiment title: Combined scattering contrast imaging of catalyst pellets under operando conditions to understand Mn promotion in Co/TiO2 Fischer Tropsch catalysts**	**Experiment number**: CH-6065
Beamline:	**Date of experiment**: from: **04 March 2022** to: **07 March 2022**	**Date of report**: 09/08/2023
Shifts:	**Local contact(s)**: Jakub Drnec	*Received at ESRF:*

Names and affiliations of applicants (* indicates experimentalists):

Prof. Andrew Michael Beale, UCL, Research Complex at Harwell, Catalysis Hub
Mr Danial Farooq, UCL, Research Complex at Harwell, Catalysis Hub

Report:

Publication

Pending publication – Processing additional XAS data to included in the paper.

Abstract

µ-XRD-CT and µ-PDF-CT techniques were used to study passivated Co/TiO_2/Mn FT catalyst recovered after reaction for 300 hrs. Increasing Mn loading (>3%) led to more cobalt carbide formation and less cobalt metal (FCC and HCP) which correlated with increasing alcohol and olefin selectivity which have commercial value. Cobalt carbide was located on the extrudates' periphery, while cobalt metal phases were at the centre, possibly due to CO diffusion limitations leading to a higher H_2/CO ratio. Reduction at a higher temperature of 450° C during preparation of a 10% Mn sample resulted in $MnTiO_3$ formation which inhibited carbide formation and alcohol selectivity. PDF analysis revealed small CoO particles at high Mn loadings undetectable by XRD. It is thought that small MnO particles promote Co carburisation by decreasing the CO dissociation barrier and the Co_2C phase promotes CO non-dissociative adsorption leading to increased oxygenate selectivity. Higher Mn loading (3-10 wt%) inhibited Co reduction which contributed to lower CO conversion and product yield. Smaller FCC/HCP particles with increasing Mn loading (1-2 wt%) contributed to improved CO conversion and C_{5+} selectivity. This study highlights the influence of Mn on catalyst structure and function and the importance of studying catalysts under industrially relevant reaction times.

Methods

Catalytic Reaction

10 %Co/TiO2 extruded trilobe pellets (radius ~ 1 mm) with varied Mn loadings (0%, 1%, 2%, 3%, 5% and 10%) were activated at 300° C and in 100% H2 at BP facilities. An additional 10% Mn sample was activated at 450° C. They were then reacted in FT conditions for 300 hrs. Conversion and selectivity were measured during the reaction. The reactor was an 8-channel high throughput unit, with common gas feeds, pressures but individual liner temperature control. 1ml of catalyst was loaded into each liner ahead of leak testing, activation and FT synthesis. The extrudates were unloaded from the reactor without removing their wax coating as a self-passivating procedure, using only a short nitrogen purge step. Samples (0%, 3% and 5% Mn) were also reacted for 150 hrs in FT conditions and recovered for analysis, using an analogous 4-channel reactor (2023). Online GC analysis was used to measure standard metrics such as conversion, short chain selectivity, and productivity as performed in a previous study (Partington et al., 2020).

XRD-CT and PDF-CT measurements

The pellets were mounted in glass capillaries (3 mm diameter and 0.1 mm wall thickness) and secured with quartz wool. The μ-XRD-CT and μ-PDF-CT scans of the extrudates were performed at ESRF, ID31. A picture of the experimental set-up is presented in Figure S1. A monochromatic pencil X-ray beam at 91 keV with a size 5 x 22 μm was used with a 50 ms acquisition time and a PILATUS CdTe 2M detector. A motorised stage was used to perform the tomographic scans with 120 translation steps over 180° (1.5° step size) utilising an interlaced approach (Vamvakeros et al., 2016). The detector was moved from 0.370 m to 1.87 m to collect both XRD and PDF data, respectively, for each cross-section of each sample. The XRD images were calibrated using a CeO_2 standard reference, which was also used to model instrumental broadening.

Tomographic Reconstruction

After calibration of every 2D diffraction image, pyFAI software (Ashiotis et al., 2015) and python scripts were used to azimuthally integrate the images to a 1D powder diffraction pattern (Vamvakeros et al., 2015). Air scattering was removed and the sinograms were centred using MATLAB scripts (MATLAB, 2020). The filtered back projection algorithm was used to reconstruct the XRD-CT data. The data was processed into a three-dimensional array (249 x 249 x 924) where the 249 x 249 pixels corresponded to the 2D cross-section image size and the 924 points stored the complete diffraction pattern for each pixel. The resultant spatial resolution of each pixel was approximately 20 μm.

XRD Refinements

TOPAS was used to perform Rietveld analysis on the XRD-CT data for quantitative phase analysis and structure determination. Initially, the CeO_2 standard was refined to find the instrumental parameters which were then fixed in the subsequent refinements. The Rietveld analysis was initially performed on the summed diffraction pattern of the entire XRD-CT data in order to arrive at a suitable starting model for subsequent sequential refinement of all the data. Scale factors were refined for each phase initially followed by lattice parameters and then crystallite size and strain parameters. Firstly, the known dominant phases, rutile and anatase, in the catalyst phase were included and refined in the input file. Next, cobalt metal phases (FCC and HCP) and cobalt carbide were refined. Due to the similar X-ray scattering effects coefficients of Mn and cobalt, cobalt and Mn oxides could not be refined separately. It is known that mixed metal oxide spinels form (Salazar-Contreras et al., 2019) which could be detected by an expansion in the lattice parameter of the cobalt oxide phases (CoO and Co_3O_4) in the refinement. The weight percentages had an error of ±0.5%, therefore a wt% of <0.5% indicated the presence of the phase could not be reliably confirmed and information on lattice parameters and crystallite size could not be extracted.

The trilobe cross-sections were divided into individual one-pixel thick layers from the outer periphery to the centre using a MATLAB script. The script searched the immediately surrounding pixels of each pixel for non-zero values to create a mask of the outermost layer of the extrudate. This layer was then subtracted, and a mask was created for the next subsequent layer. This process was repeated until all layers were characterised with a mask. These individual layers were summed, and Rietveld refined using TOPAS to investigate the chemical structure as a function of the distance from the pellet centre. 2D spatial maps of the refinement results were produced.

Generating the PDF and Real-space Refinements

The atomic pair distribution function (PDF) was produced by Fourier transforming the XRD-CT data using PDFGetX3 software (Juhas et al., 2013) which also performed various additive and multiplicative corrections, for instance due to finite Q range and atomic scattering factors. The PDFs were calculated to a Q_{max} of 25.3 $Å^{-1}$ and to a r value of 50 Å with a $Q_{maxinst}$ parameter of 25.3 $Å^{-1}$. Initially, the mean XRD pattern was transformed into a mean PDF pattern and analysed to build a good starting model for the subsequent sequential refinement that would be performed. Real-space Rietveld refinement was performed using TOPAS (Coelho, 2018) which

minimises a residual between the experimental PDF and a calculated PDF using a least-squares optimisation approach. Various macros were used to implement PDF real-space refinement on TOPAS (Yang et al., 2020)(Dinnebier et al., 2018). Firstly, peak broadening and dampening due to instrument factors were refined using the CeO_2 standard which were subsequently fixed for the refinement of the PDF of the sample. Scale, crystallite size, lattice parameters and atomic displacement parameters (B_{eq}) were refined sequentially for the mean pattern. There is a gradual dissipation of correlated motion as a function of *r* and this was included in the refinement by modelling the atomic displacement parameters using a spherical function. Screening of additional structures that were potentially present in the sample was carried out using a web-based programme, 'PDF in the Cloud' (Yang et al., 2020). The programme enabled automated structure refinements to be carried out, using CIF files sourced from a crystallographic server. The refinements were carried out on difference PDF's that were obtained from the difference between the experimental data and the known refined support phases, anatase and rutile, and cobalt phases to determine if any unexpected phases were present. Like in the XRD processing, separate layers from the extrudate trilobes were transformed into PDF's and refined to further study the extrudate structure as a function of distance from the centre of the pellets. The results were then processed in to 2D phase spatial maps using MATLAB.

Results

Mean XRD-CT pattern Refinement

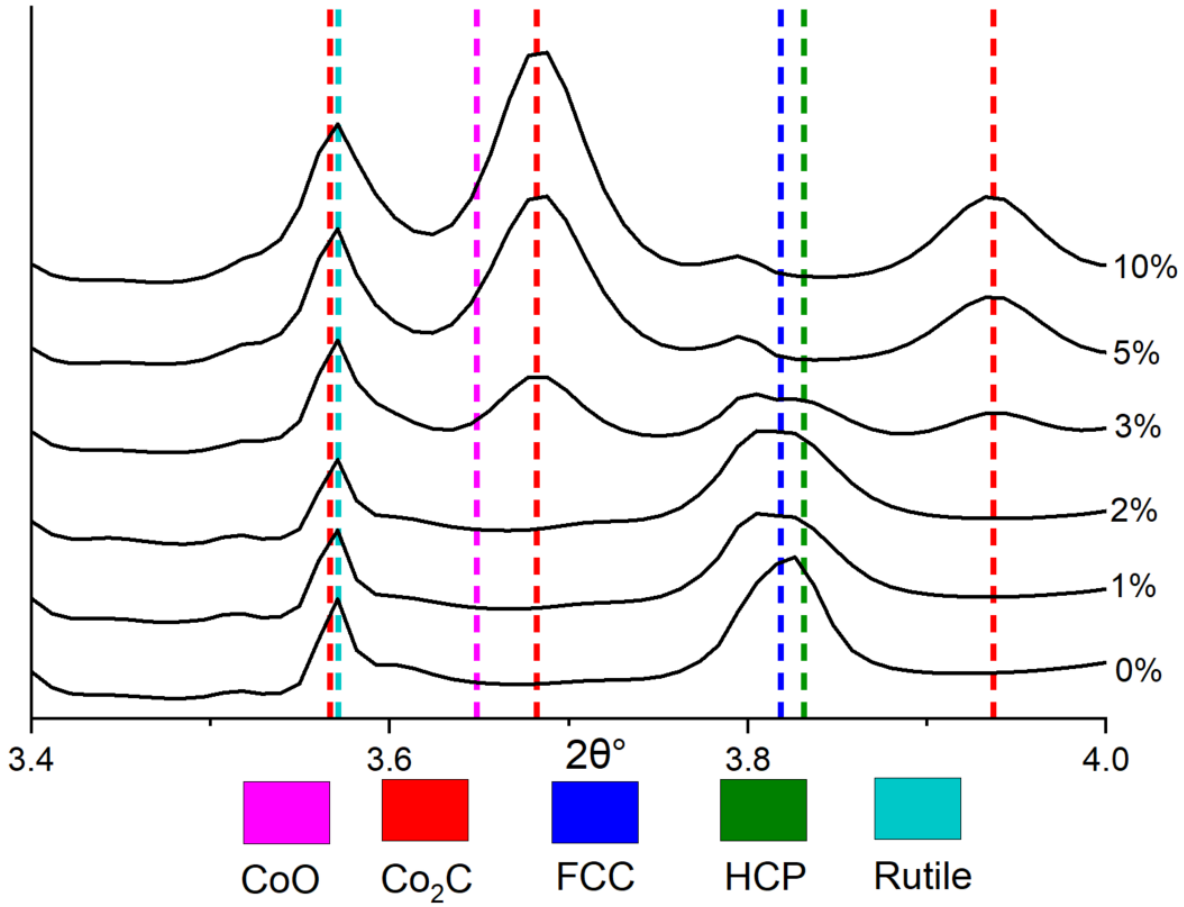

Figure 1 - Stacked Mean XRD-CT patterns of all the different samples with varied Mn loading showing the increasing cobalt carbide content with increasing Mn loading and the concomitant loss of the Co metal phases (FCC and HCP). Low wt % of CoO was present in the higher Mn loading samples (5% and 10% Mn). Note that no reflections due to the anatase TiO_2 polymorph are present in this portion of the diffraction pattern.

The mean XRD-CT refined patterns for the samples are illustrated in Figure 1 and the results are presented in Table 1. It is found that the Co_2C phase increased with Mn loading whilst the Cobalt metal phases (FCC and HCP) both decreased. The Co was mostly reduced in the Co-containing species as the samples were recovered

from the reactor under predominantly reducing conditions and the wax products remaining on the catalysts prevented oxidation. There was, however, a small percentage (3 wt%) of CoO detected in the 10% Mn sample with an expanded lattice parameter (4.29Å). MnO was not refined separately in addition to CoO as Co and Mn have similar scattering factors and so they cannot be differentiated by Rietveld refinement. Previous research has pointed towards the presence of mixed-oxide spinels with an expanded lattice parameter ($Co_{1-x}Mn_xO$) (Paterson et al., 2020, Liu et al., 2019). Consistent with previous work, no crystalline Mn-containing species were detected (Paterson et al., 2020). The mean pattern in Figure S2 illustrates the presence of the different phases in the 3% sample which contains the Co^0 metal phases (FCC and HCP) and the Co_2C phase as well as the difference between the refined and experimental data. The FCC (200) peak was excluded from the refinements as it was not present due to the possible present of stacking faults. Whilst this aided the fit of the FCC (100) peak, the presence of stacking faults results in more complex peak shapes and asymmetry that would require more elaborate modelling to improve the fit further. The full pattern is presented in Figure S3, where the support phases (TiO_2), anatase and rutile, were identified whilst $MnTiO_3$ was formed in the 10% Mn sample reduced at 450°C.

The Co_2C phase wt% increased with Mn loading from 3% until 10% and was at trace values at 1% and 2% loadings where it was just at 1.1%. The crystallite size of the Co^0 FCC phase was found to decrease with increasing Mn loading which correlates with previous research (Paterson et al., 2018). The total Cobalt metal (FCC + HCP + Co_2C) wt% was found to vary where it was around 7% at 0-2% Mn loadings but 8-10% at 3-5% weight loadings. This suggests that some of the cobalt is not found in the XRD at low Mn wt% loadings due to small crystallite sizes or disordered cobalt being present. CoO is present at very small wt % (0.5-2%) suggesting that nearly all the cobalt is reduced, validating the wax passivation method of the catalyst.

A 5% Mn sample was extracted after 150 hrs of reaction, and it was found that the Co_2C phase had formed at this intermediate stage. However, the refined weight percentage of the Co_2C phase increased from 7.5% at 150 hrs to 8.9% at 300 hrs and the crystallite size increased from 7.5 nm to 9.3 nm indicating that the Co was further carburised during this period.

Table 1 - Rietveld Refinement results of the XRD-CT mean patterns illustrating the phase wt %, CS (crystallite size in nm) and LP (lattice parameters) of the samples extracted after 150 hrs and 300 hrs. The Co_2C wt % increases with Mn loading whilst the Co^0 metal phases (FCC and HCP) decrease with increasing Mn wt% beyond 5%. The 10%[a] samples were reduced at 450° C which resulted in the production of Mn titanates ($MnTiO_3$).

[a] Reduction at 450° C

Phase		**Mn wt %**							
Hrs		**150**				**300**			
		5%	**0%**	**1%**	**2%**	**3%**	**5%**	**10%**	**10%[a]**
R_{wp} (%)		6.4	6.9	6.2	6.2	6.2	6.7	7.9	7.9
Co_2C	Wt%	7.5	-	0.6	0.9	3.6	8.9	7.1	-
	CS	7.5	-	10.8	6.5	10.6	9.3	11.7	-
	LP	2.89	-	2.99	2.99	2.89	2.89	2.89	-
	(Å)	4.45	-	4.61	4.65	4.45	4.45	4.45	-
		4.37	-	4.28	4.26	4.37	4.37	4.37	-
HCP	Wt %	0.2	4.9	4.8	3.8	3.1	0.2	0.7	5.3
	CS	-	2.6	2.2	2.2	7.1	-	9.9	2.9
	LP	2.51	2.51	2.51	2.52	2.51	2.51	2.50	2.51
	(Å)	4.10	4.10	4.10	4.06	4.08	4.01	4.21	4.08
FCC	Wt%	0.4	3.5	3.3	3.6	1.6	0.1	0.0	2.9
	CS	3.54	10.5	8.1	7.7	5.2	-	-	11.2
	LP (Å)	3.54	3.54	3.54	3.54	3.54	-	-	3.54
CoO	Wt%	0.9	0.3	0.1	0.2	0.5	1.2	3.1	0.4
	CS	4.0	7.1	3.0	3.7	3.1	3.3	2.6	5.7
	LP (Å)	4.22	4.28	4.26	4.27	4.24	4.24	4.29	4.28

Anatase	Wt%	80.2	77.8	78.4	80.1	79.7	78.9	80.3	65.1
	CS	16.9	21.4	20.7	19.8	19.5	18.9	13.7	15.1
	LP	3.79	3.79	3.79	3.79	3.79	3.79	3.79	3.79
	(Å)	9.51	9.50	9.51	9.50	9.50	9.50	9.50	9.50
Rutile	Wt%	10.8	13.5	12.8	11.4	11.4	10.8	8.8	2.6
	CS	25.8	42.6	40.8	39.6	38.2	37.4	28.6	29.1
	LP	4.60	4.59	4.59	4.59	4.59	4.59	4.60	4.60
	(Å)	2.96	2.95	2.96	2.96	2.96	2.96	2.96	2.96
$MnTiO_3$	Wt%								23.7
	CS								20.8
	LP								5.14
	(Å)								14.26

XRD-CT Refinement

The XRD-CT spatial maps presented in Figure 2 illustrate the increasing Co_2C content present on the periphery of the catalytic extrudates with increasing Mn loading above 3 wt %. This indicates a promotional effect of the Mn at loadings of 3 wt% and higher which facilitates cobalt carbide production in the active catalyst. Furthermore, it is found that the Co metal (FCC and HCP) phases were present uniformly at lower Mn loadings but in the centre of the extrudates at higher loadings. Slightly more HCP phase (~1 wt%) is present than the FCC phase in the active catalyst and increased Mn loading from 0-2% is shown to result in more uniform distribution of the FCC phase. FCC and HCP cobalt phases were both present in the 10% Mn (reduced at 450° C) sample and there was no presence of carbides, exhibiting a similar distribution of phases as the 0% sample. This is due to the Mn being locked away in the Mn titanate phase which prevents its promotional effects that require the Mn to be close to the cobalt. Figure 3 shows the XRD patterns of successive layers in the 3% Mn catalyst where it can be seen how the Co_2C phase is present at the periphery of the extrudates whereas the FCC and HCP cobalt metal phases are present at the centre. Only a small percentage of CoO was found to be present indicating that most of the cobalt was reduced however more was found to be present at higher Mn loadings, though just around 2 wt %. The R_{wp} (residual weight percentage) was relatively constant at around 7-8% indicating a good fit for all the patterns. However, a higher R_{wp} at 9% occurred in the 3% Mn sample, which could be due to the error associated with the transition between the Co_2C and HCP phases from the periphery to the centre.

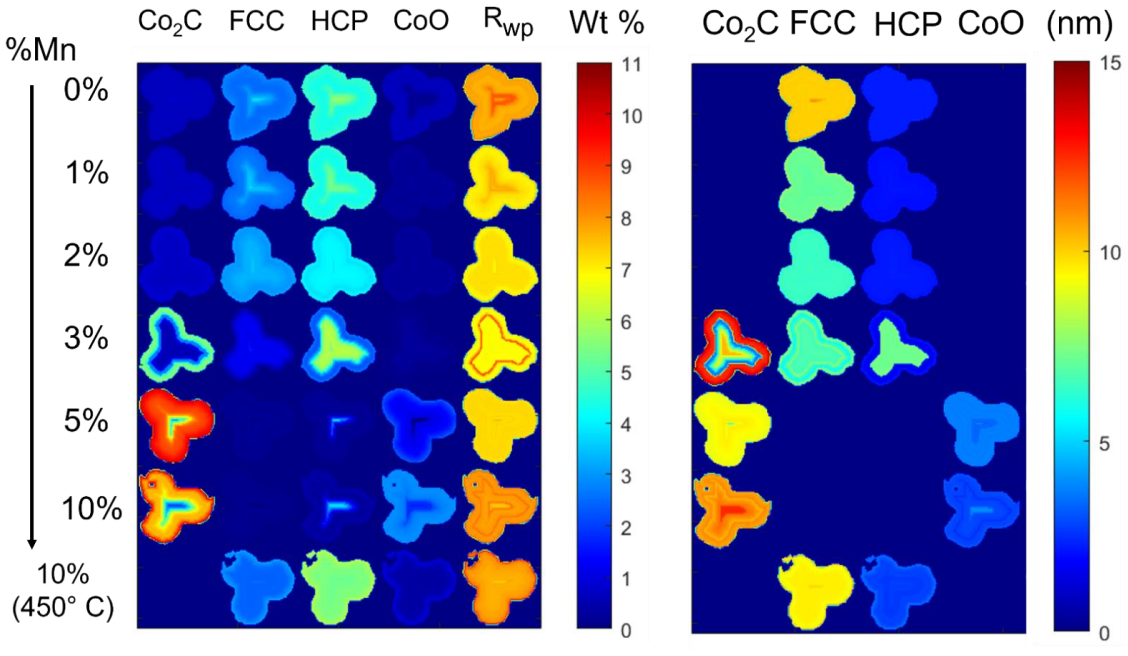

Figure 2 - Reconstructed XRD-CT 2D images of the catalytic pellets (extracted after 300 hrs) illustrating the refined wt % percentage (left) and crystallite size (right) of the different phases present. Increased Mn loading resulted in more

cobalt carbide and a smaller particle size of the FCC phase. Lower Mn loadings had a higher presence of FCC and HCP phases. An egg-shell distribution is observed with Co_2C egg-white and HCP in the centre.

It was found that the FCC crystallite size decreases with increasing Mn loading as seen in **Error! Reference source not found.** which corresponds to previous research (Paterson et al., 2020). The particle sizes of the HCP phase (2.5nm) are much smaller than the FCC phase (6-10nm) except for in the 3% Mn catalyst where larger HCP particles are found to be formed at the centre of the extrudates. Larger Co_2C particles (14nm) are found to be formed on the periphery of the 3% Mn catalyst compared to the 5% and 10% Mn catalysts (10nm). This agrees with previous research that found that Mn in close proximity to larger cobalt particles would carburize (van Koppen et al., 2022). Small CoO particles are found to be present at higher Mn loadings (5% and 10%), which are expected to be mixed-oxide spinels ($Co_{1-x}Mn_xO$), indicating that the Mn inhibited reduction of Co. The phase distribution and crystallite sizes did not vary significantly with height and XRD-CT cross-section maps of the samples at different heights are presented in Figure S4.
Spatial maps of the wax were produced (Figure S5) by refining polypropylene (CH_2) and it was found that that more wax content remained on the catalyst with increasing Mn loading. This correlates with research that found that olefin products are more likely to readsorb on the catalyst surface, due to greater solubility in synthesis liquids, and undergo secondary reactions such as hydrogenation (Iglesia et al., 1991, Iglesia, 1997).

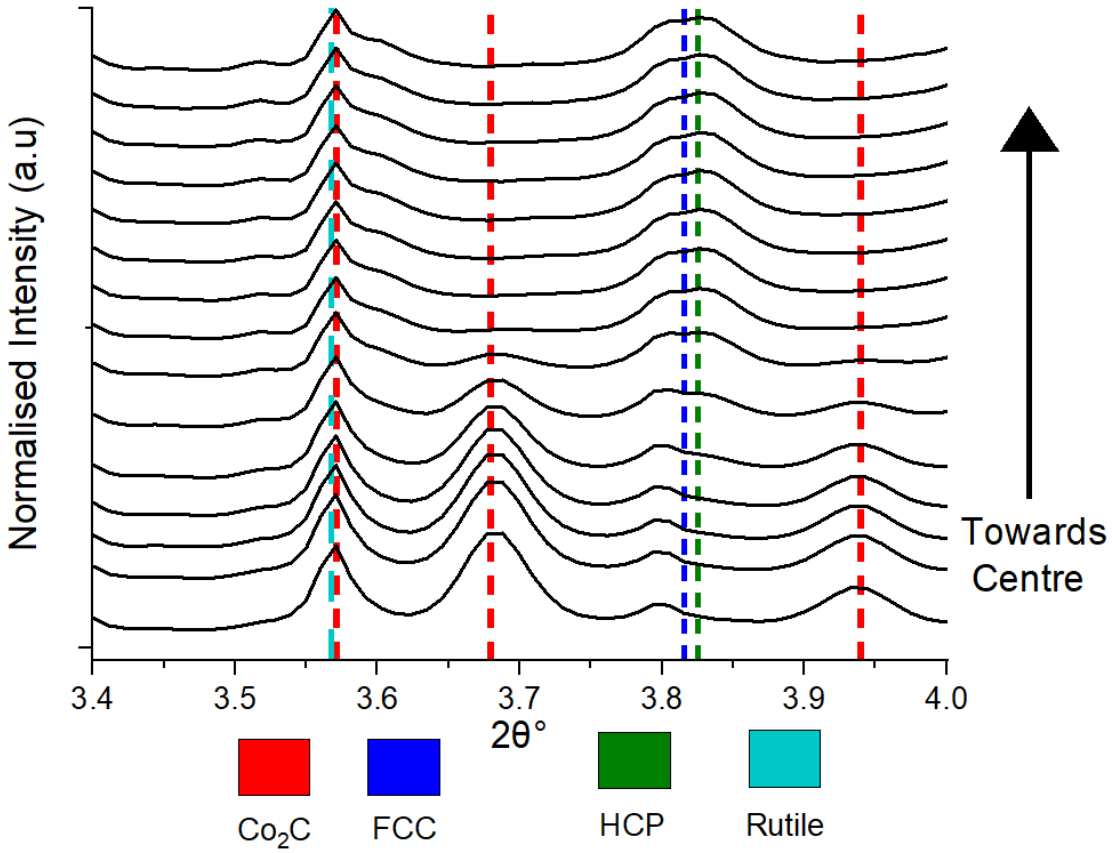

Figure 3 - Stacked XRD patterns of the successive layers of the 3% Mn catalyst extrudate showing the evolution of the different cobalt phases with increasing distances (20µm steps) from the centre of the catalyst pellet. Co_2C is present at the surface periphery whilst FCC and HCP phases are present at the centre.

Mean PDF Refinement

The summed PDF patterns were produced by summing all the Bragg data for each pixel and then Fourier transforming the result. Similar to the XRD refinement, an increase in Mn loading resulted in increased Co_2C formation, first appearing at 3 wt % Mn, whilst Co^0 (FCC and HCP) phases were present at lower Mn loadings (0% and 1%). There was a higher percentage of FCC/HCP cobalt detected in the PDF than in the XRD indicating the presence of small cobalt metal particles. A larger percentage of CoO is detected at higher Mn wt % indicating that the Mn was present in disordered or small mixed-oxide spinels ($Co_1Mn_{1-x}O$) particles that

could not be detected by XRD. The refinement of the mean patterns from 0-10 Å is presented in Figure S6 where there are changes to the Co-Co peak at 2.5 Å due to the formation of cobalt carbide.

Table 2 - Rietveld Refinement results of the PDF-CT mean patterns illustrating the phase wt %, CS (crystallite size) and LP (lattice parameters). The results correlate well with the XRD refinement. Co2C wt % increases with Mn loading whilst the Co0 metal phases (FCC and HCP) decrease with increasing Mn wt% beyond 5%.

[a] Reduction at 450° C

Phase	Parameter	Mn wt %					
		0%	**1%**	**3%**	**5%**	**10%**	**10%[a]**
	R_{wp}(%)	21.6	21.5	21.1	22.1	23.5	25.8
Co_2C	Wt%	1.1	1.1	3.7	9.1	9.5	1.3
	CS (nm)	-	-	-	15.6	12.0	-
	LP (Å)	2.87	2.87	2.88	2.88	2.88	2.87
		4.41	4.42	4.43	4.43	4.43	4.42
		4.39	4.39	4.37	4.37	4.37	4.39
HCP	Wt %	5.0	4.8	5.4	0.3	0.2	2.2
	CS (nm)	3.9	3.6	4.2	-	-	5.6
	LP (Å)	2.49	2.50	2.50	2.58	2.60	2.73
		4.09	4.09	4.07	4.04	4.05	3.96
FCC	Wt%	5.7	5.4	1.7	0.2	0.0	5.0
	CS (nm)	4.0	3.7	4.1	-	-	8.5
	LP (Å)	3.53	3.54	3.54	3.59	3.59	3.53
CoO	Wt%	1.1	1.1	1.0	1.1	5.2	1.7
	CS (nm)	21.3	19.4	16.1	11.4	1.0	2.6
	LP (Å)	4.25	4.26	4.26	4.26	4.34	4.29
Anatase	Wt%	71.1	72.1	74.0	76.2	73.2	59.3
	CS (nm)	5.1	5.1	5.0	5.0	4.5	4.6
	LP (Å)	3.78	3.78	3.78	3.78	3.78	3.78
		9.47	9.47	9.47	9.47	9.47	9.47
Rutile	Wt%	15.8	15.2	13.9	12.8	11.6	5.2
	CS (nm)	4.3	4.4	4.4	4.6	4.2	4.6
	LP (Å)	4.59	4.59	4.59	4.59	4.60	4.62
		2.95	2.95	2.95	2.95	2.94	2.91
$MnTiO_3$	Wt%						25.8
	CS (nm)						9.30
	LP (Å)						5.12
							14.23

PDF-CT Refinement

The results from the PDF-CT refinement correlated with the results from the XRD-CT refinement where an increasing Mn loading was found to lead to an increase in Co_2C formation on the extrudate periphery and decreasing Co^0 (FCC and HCP) content in the centre. The PDF-CT wt % maps are presented in Figure 4 whilst the crystallite size maps are presented in **Error! Reference source not found.**. A higher wt % of CoO is found in the PDF than in the XRD, possibly due to the small average particle size (1 nm) not being detected. The CoO wt % is shown to increase with increasing Mn loading which is understood to be due to the incorporation of Mn in the CoO lattice forming $Co_xMn_{1-x}O$ spinels. Similar to the XRD results, the crystallite

size of the FCC particles was found to decrease with increasing Mn loading, correlating with previous research (Paterson et al., 2020). However, large HCP particles were found in the centre of the extrudates at higher Mn loadings.

The R_{wp} is multiplied by a factor of one third in the maps in order to visually identify any abnormalities and correlation. It is found that the error is uniform throughout at around 30 %. The errors in real-space PDF refinements are usually higher than those in XRD and this R_{wp} value is tolerable and indicates a reasonable fit.

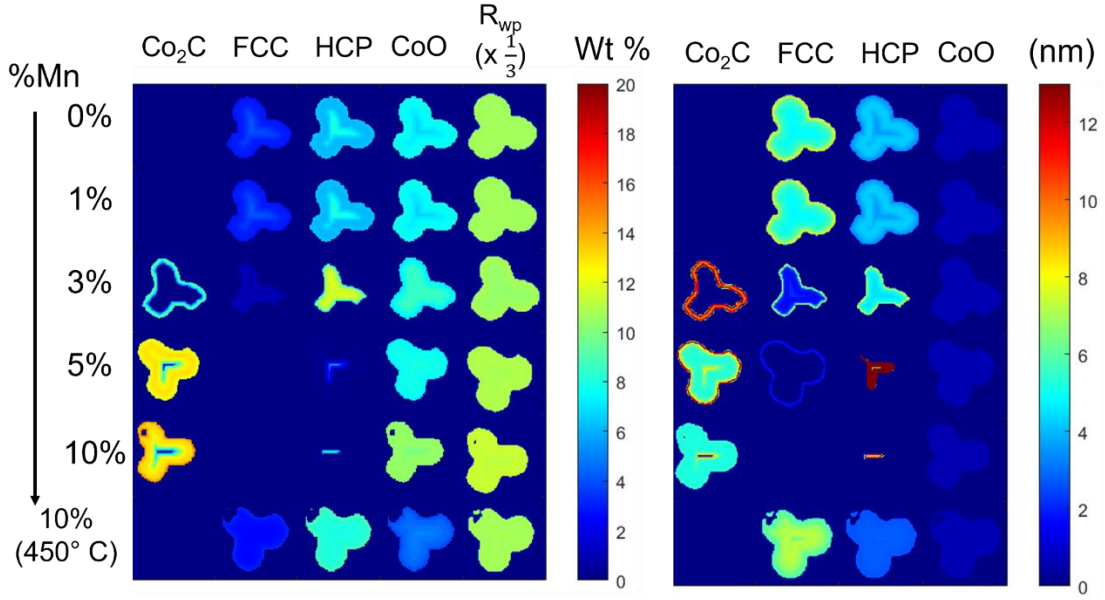

Figure 4 - Reconstructed PDF-CT 2D images of the catalytic pellets illustrating the refined wt % percentage (left) and crystallite size (right) of the different phases present in each pixel of the catalyst pellet for the different Mn loadings. Small CoO particles were present at higher Mn loadings whilst large HCP crystals were present at the centre of the 3% Mn sample.

Product Analysis

Catalyst stability was investigated throughout the reaction and the results for the 2% Mn catalyst are presented in Figure 5 where it was found that activity and selectivity was relatively constant from 160-300 hrs. The CO conversion and product selectivity for olefins, alcohols and C_{5+} was measured throughout the reaction for 160 - 300 hrs and is presented in Figure 5 as averages for all the samples. The average CO conversion of the 2% Mn sample was the highest (49%) whilst the 1% Mn sample was marginally lower at 46%. This indicates that the Mn promoter improved conversion, even at low weight percentages, possibly due to the smaller crystallite size of the FCC/HCP Co phases. However, at increasing Mn loading (5-10%), conversion was also lower at 36%. The 10% Mn sample which was reduced at 450° C had an average conversion rate at 38% throughout the experiment which was similar to the 0% sample.

Product selectivity for olefins, alcohols and C_{5+} was measured for the different catalytic systems throughout the reaction and is presented in Figure 6. The 1% and 2% Mn catalysts exhibited high C_{5+} selectivity and low olefin and alcohol selectivity. The catalysts with higher Mn loadings (3-10%) demonstrated higher alcohol and olefin selectivity but lower C_{5+} selectivity. The 3% Mn catalyst had the highest alcohol and olefin selectivity and the lowest C_{5+} selectivity. The 10% Mn catalyst which was reduced at 450° C showed similar selectivity as the 0% Mn catalyst due to the Mn being locked away in Mn titanates.

C_{5+} selectivity was the highest for the 1% and 2% Mn catalysts (77-80%) suggesting that the Mn promoted chain growth at low weight percentages. This is expected to be due to the smaller crystallite size of the FCC/HCP Co phases for these samples. However, at higher weight percentages of Mn (3-10%) the selectivity was much lower, and this correlated with an increase in alcohol and olefin selectivity. The selectivity to olefins and alcohols was highest for the 3% Mn sample and much lower for the 0-2% Mn samples. The samples with higher Mn loadings (5-10 wt %) showed lower olefins and alcohols selectivity than the 3% sample but higher than the 0-2% Mn samples. The Mn promotes olefin and alcohol formation the most in the 3% sample and to a lesser extent at higher Mn loadings. This indicates that the reduced amount of Co^0 metal plays a role in reducing olefin and alcohol selectivity in the higher loading Mn catalysts.

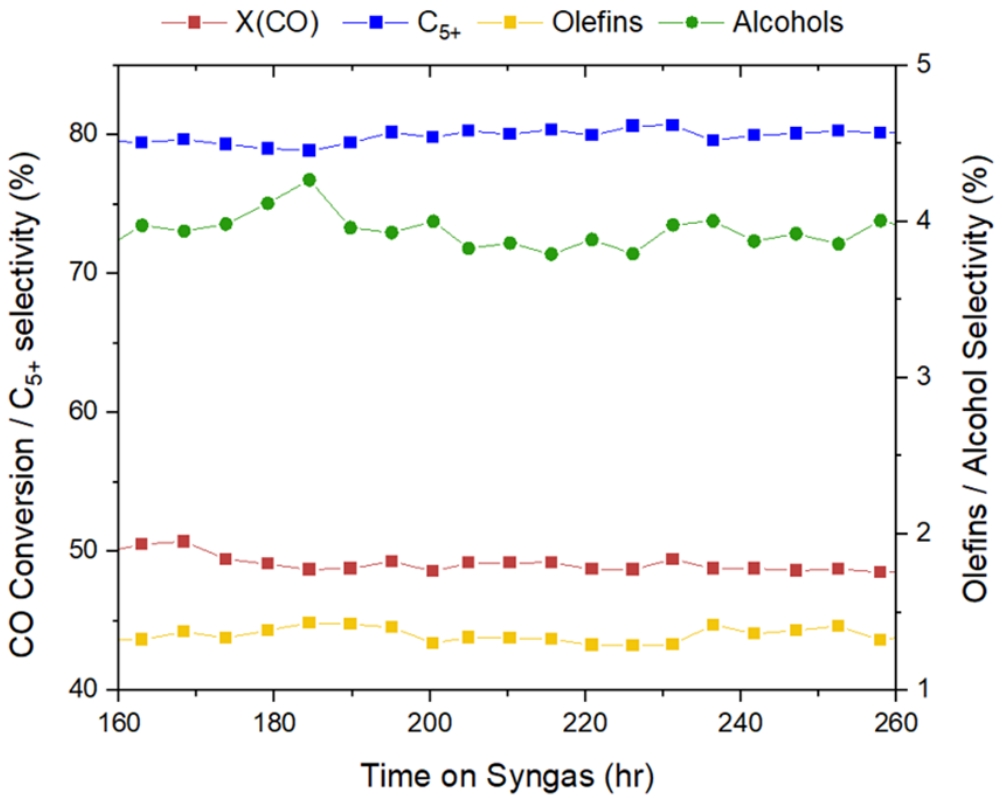

Figure 5 – CO conversion and selectivity to C_{5+}, alcohols and olefins for the 2% Mn sample for the reaction time from 160 to 300 hrs. The selectivity and conversion are stable with time on stream.

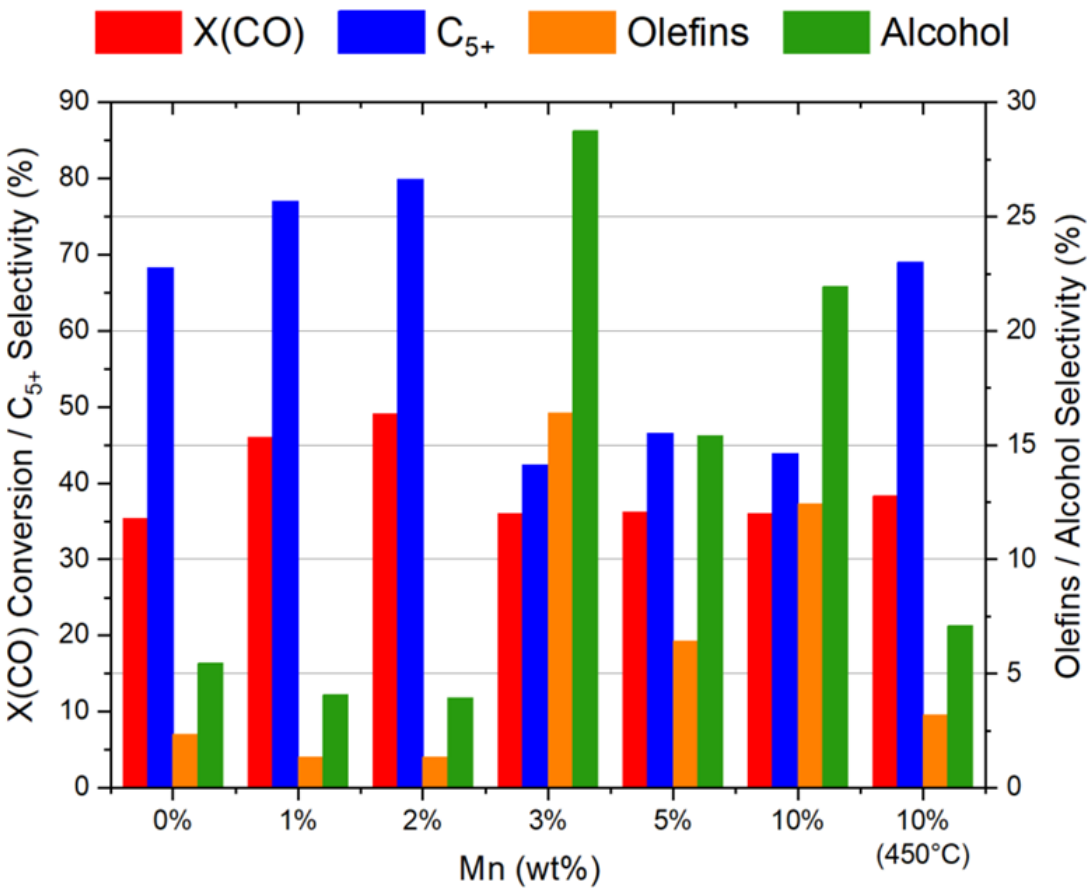

Figure 6 – CO conversion and C_{5+}, alcohol and olefin selectivity as a function of Mn loading. It is found that an increase in Mn (wt%) results in an increase in C_{5+} selectivity from 0-2%, and increased alcohol and olefin selectivity except for the 10% Mn sample reduced at 450°C.

Summary and Conclusion

µ-XRD-CT and µ-PDF-CT techniques were used as complementary techniques to study $Co/TiO_2/Mn$ FT catalyst where it was found that increasing Mn loading corresponded to increasing cobalt carbide content and decreasing cobalt metal (FCC and HCP) in passivated catalyst recovered after reaction. It was found that the cobalt carbide was located on the periphery of the catalytic extrudates whilst the cobalt metal phases (FCC and HCP) were at the centre. This could be due to a higher partial pressure of CO at the periphery due to pore diffusion limitations of the syngas. It has been found that Co_2C is formed inversely proportionally to the H_2/CO ratio (Claeys et al., 2014). Evidence has also shown that before reduction, aggregated cobalt oxide particles (weak metal-support interactions) which are preferably located at the edges of the extrudates reduce more quickly (Senecal et al., 2017). This was suggested due to a higher H_2 concentration at the centre and particle size effects. A sudden increase in alcohol and olefin selectivity at 3% Mn coincides with an increased amount of Co_2C indicating that the carbide phase is active. More research is required to understand the exact mechanism that leads to the selectivity changes. It is thought that the Mn leads to a decrease of the CO dissociation barrier promoting carburisation of cobalt (Paterson et al., 2020). Furthermore, DFT calculations have found that Co_2C promotes CO non-dissociative adsorption leading to increased oxygenate selectivity (Pei et al., 2015). The production of Mn titanates ($MnTiO_3$), due to reduction at 450°C, changes the selectivity of the high loading 10% Mn catalyst to that of a 0% Mn catalyst, where there is higher C_{5+} but lower olefins and alcohol selectivity. The Mn is locked away in Mn titanates and is not able to promote cobalt carbide formation leaving the cobalt metal in the FCC and HCP form.

PDF analysis does not assume periodic order and allows the study of small nanoparticles and disordered phases that are not detectable using XRD. PDF-CT revealed the presence of small CoO particles (~1.5 nm) at high Mn loadings indicating the presence of mixed oxide spinels ($Co_xMn_{1-x}O$). This suggests that Mn inhibits Co reduction which led to decreased CO conversion and product yield. Slightly higher weight percentages of FCC/HCP phases were found using PDF indicating that a small proportion were present as small nanoparticles that could not be found in the XRD refinements.

Recovering and imaging the catalyst after 300 hrs of reaction provided an insight into the catalytic structure during industrially relevant conditions and timescales. This enabled the study of the formation of the cobalt carbide phase as a function of Mn loading with spatial resolution by using XRD-CT and PDF-CT chemical imaging techniques.

Future Work

- Analysis of the presence of stacking faults in the $Co/TiO_2/Mn$ catalyst.
- Investiating the role of Mn in the formation of Co_2C in the catalytic systems.
- The use of different supports and the formation of carbides with alcohol/olefin selectivity.
- Formation of carbides with different syngas ratios during reduction and reaction.

References

2023. *hte provides high throughput unit for syngas conversion to bp* [Online]. Germany: hte company. Available: https://www.hte-company.com/en/news-events/news/news-with-bp-1 [Accessed 04/07/2023 2023].
ASHIOTIS, G., DESCHILDRE, A., NAWAZ, Z., WRIGHT, J. P., KARKOULIS, D., PICCA, F. E. & KIEFFER, J. 2015. The fast azimuthal integration Python library: pyFAI. *Journal of applied crystallography,* 48**,** 510-519.
CLAEYS, M., DRY, M., VAN STEEN, E., DU PLESSIS, E., VAN BERGE, P., SAIB, A. & MOODLEY, D. J. J. O. C. 2014. In situ magnetometer study on the formation and stability of cobalt carbide in Fischer–Tropsch synthesis. 318**,** 193-202.
IGLESIA, E. 1997. Design, synthesis, and use of cobalt-based Fischer-Tropsch synthesis catalysts. *Applied Catalysis A: General,* 161**,** 59-78.
IGLESIA, E., REYES, S. C. & MADON, R. J. J. J. O. C. 1991. Transport-enhanced α-olefin readsorption pathways in Ru-catalyzed hydrocarbon synthesis. 129**,** 238-256.
LIU, S., SUN, B., ZHANG, Y., LI, J., RESASCO, D. E., NIE, L. & WANG, L. 2019. The role of intermediate Co x Mn 1− x O (x= 0.6–0.85) nanocrystals in the formation of active species for the direct production of lower olefins from syngas. *Chemical Communications,* 55**,** 6595-6598.
MATLAB 2020. 9.7.0.1190202 (R2020b). Natick, Massachusetts: The MathWorks Inc.
PARTINGTON, R., CLARKSON, J., PATERSON, J., SULLIVAN, K., WILSON, J. J. J. O. A. S. & TECHNOLOGY 2020. Quantitative carbon distribution analysis of hydrocarbons, alcohols and carboxylic acids in a Fischer-Tropsch product from a Co/TiO 2 catalyst during gas phase pilot plant operation. 11**,** 1-20.
PATERSON, J., PARTINGTON, R., PEACOCK, M., SULLIVAN, K., WILSON, J. & XU, Z. 2020. Elucidating the Role of Bifunctional Cobalt-Manganese Catalyst Interactions for Higher Alcohol Synthesis. *European Journal of Inorganic Chemistry,* 2020**,** 2312-2324.
PATERSON, J., PEACOCK, M., PURVES, R., PARTINGTON, R., SULLIVAN, K., SUNLEY, G. & WILSON, J. 2018. Manipulation of Fischer-Tropsch Synthesis for Production of Higher Alcohols Using Manganese Promoters. *ChemCatChem,* 10**,** 5154-5163.
PEI, Y.-P., LIU, J.-X., ZHAO, Y.-H., DING, Y.-J., LIU, T., DONG, W.-D., ZHU, H.-J., SU, H.-Y., YAN, L. & LI, J.-L. J. A. C. 2015. High alcohols synthesis via Fischer–Tropsch reaction at cobalt metal/carbide interface. 5**,** 3620-3624.
SENECAL, P., JACQUES, S. D. M., DI MICHIEL, M., KIMBER, S. A. J., VAMVAKEROS, A., ODARCHENKO, Y., LEZCANO-GONZALEZ, I., PATERSON, J., FERGUSON, E. & BEALE, A. M. 2017. Real-Time Scattering-Contrast Imaging of a Supported Cobalt-Based Catalyst Body during Activation and Fischer–Tropsch Synthesis Revealing Spatial Dependence of Particle Size and Phase on Catalytic Properties. *ACS Catalysis,* 7**,** 2284-2293.
VAMVAKEROS, A., JACQUES, S. D., DI MICHIEL, M., MIDDELKOOP, V., EGAN, C. K., CERNIK, R. J. & BEALE, A. M. 2015. Removing multiple outliers and single-crystal artefacts from X-ray diffraction computed tomography data. *Journal of Applied Crystallography,* 48**,** 1943-1955.
VAMVAKEROS, A., JACQUES, S. D. M., DI MICHIEL, M., SENECAL, P., MIDDELKOOP, V., CERNIK, R. J. & BEALE, A. M. 2016. Interlaced X-ray diffraction computed tomography. *Journal of Applied Crystallography,* 49**,** 485-496.
VAN KOPPEN, L. M., DUGULAN, A. I., BEZEMER, G. L. & HENSEN, E. J. J. J. O. C. 2022. Sintering and carbidization under simulated high conversion on a cobalt-based Fischer-Tropsch catalyst; manganese oxide as a structural promotor. 413**,** 106-118.
YANG, L., JUHÁS, P., TERBAN, M. W., TUCKER, M. G. & BILLINGE, S. J. 2020. Structure-mining: screening structure models by automated fitting to the atomic pair distribution function over large numbers of models. *Acta Crystallographica Section A: Foundations and Advances,* 76**,** 395-409.